Experiments in Fluids 25 (1998) 108–117 © Springer-Verlag 1998

Measurement of unsteady boundary layer developed on an oscillating airfoil using multiple hot-film sensors

T. Lee, S. Basu

Abstract The spatial-temporal progressions of the leading-edge stagnation, separation and reattachment points, and the state of the unsteady boundary layer developed on the upper surface of a 6 in. chord NACA 0012 airfoil model, oscillated sinusoidally within and beyond the static-stall angle, were measured using 140 closely-spaced, multiple hot-film sensors (MHFS). The MHFS measurements show that (i) the laminar separation point and transition were delayed with increasing α and the reattachment and relaminarization were promoted with decreasing α, relative to the static case, (ii) the pitchup motion helped to keep the boundary layer attached to higher angles of attack over that could be obtained statically, (iii) the dynamic stall process was initiated by the turbulent flow separation in the leading-edge region as well as by the onset of flow reversal in the trailing-edge region, and (iv) the dynamic stall process was found not to originate with the bursting of a laminar separation bubble, but with a breakdown of the turbulent boundary layer. The MHFS measurements also show that the flow unsteadiness caused by airfoil motion as well as by the flow disturbances can be detected simultaneously and nonintrusively. The MHFS characterizations of the unsteady boundary layers are useful in the study of unsteady separated flowfields generated by rapidly maneuvering aircraft, helicopter rotor blades, and wing energy machines.

List of symbols

C	chord
f_0	oscillation frequency
Re	chord Reynolds number, $=CU_0/\nu$
S	spacing between each hot-film sensor or distance along the surface of the airfoil from the leading-edge stagnation point
t	time
U_0	free-stream velocity
rms	root-mean-squared value
τ	time scale, $=\omega t$
κ	reduced frequency, $=\omega C/2U_0=\pi f_0 C/U_0$
ν	kinetic viscosity of fluid
α_{SS}	static stall angle
$\alpha(t)$	instantaneous angle of attack, $=\alpha_0+\Delta\alpha\sin\omega t$
α_0	mean angle of attack
$\Delta\alpha$	oscillation amplitude
ω	angular frequency, $=2\pi f_0$

1
Introduction

The characterization and potential utilization of unsteady separated flows constitute a challenging area of fluid mechanics. A particular important example is the pitching airfoil problem which has practical applications to helicopter rotor blades, aircraft maneuverability, wind turbines, and jet engine compressor blades. Frequently, unsteady separated flows exercised a pronounced adverse influence upon the effectiveness of these and other systems. If thoroughly understood and properly controlled, unsteady separated flows could be eliminated or even harnessed, thereby dramatically enhancing performance for a broad spectrum of fluid dynamic systems. However, the characterization of the behavior of the unsteady boundary layer developed on airfoils in unsteady motion is complicated by the need to account for many interrelated flow parameters, such as Mach number, Reynolds number, type of unsteadiness (plunging, pitching, or translation), waveform (sinusoidal, constant-rate ramp, or arbitrary), amplitude, and frequency (or pitch rate). In particular, the response during dynamic stall may differ substantially, depending upon whether the boundary layer prior to separation is laminar or turbulent, fully attached or containing regions of reversed flow. Recent reviews on unsteady aerodynamics and dynamic stall are given by McCroskey (1982) and Carr (1987).

However, in order to advance the understanding of the unsteady flows developed or aerodynamic objects in unsteady motion, and to continue the development and validation of predictive methods, detailed measurement of the nature of the unsteady boundary layer is a prerequisite. Experimental techniques, such as hot-wire anemometry, single and dual heated wall-shear-stress gages, laser Doppler velocimetry (LDV) with frequency shifting, surface pressure transducers, and various qualitative flow visualization methods, have been used to investigate the unsteady boundary-layer events (which include flow separation and reattachment, boundary-layer transition and flow reversal) developed on airfoils oscillating beyond and within its static-stall angle (McCroskey et al. 1976, 1977; McAlister and Carr 1979; Daley and Jumper 1984; Favier et al. 1988; Koochesfahami 1989; Lorber et al. 1988, 1992, 1994;

Received: *17 June 1997*/*Accepted*: *10 December 1997*

T. Lee
Department of Mechanical Engineering, McGill University
Montreal, Quebec, Canada

This work was supported by the Natural Sciences and Engineering Research Council of Canada (NSERC).

Chandrasekhara and Ahmed 1991; Ohmi et al. 1991; Acharya and Metwally 1992; Schreck et al. 1994).

However, the hot-wire anemometry could be intrusive and provides only pointwise flowfield information. The single or dual-heated hot-film sensors are nonintrusive and have first been used primarily as a skin friction indicator pointwise (Bellhouse and Schultz 1966), and to determine stages of laminar-to-turbulence transition process which can be sensitively influenced by intrusive probes (Bellhouse and Schultz 1966; Owen and Bellhouse 1970). Their measuring principle is based on convective heat loss into the fluid from the heated films and consequently responds in a quantitative way to fluctuations in local shear stress. The nonintrusive LDV system is, in general, sophisticated and relatively expensive. The surface pressure measurement technique has been used extensively to obtain the integrated aerodynamic loads, as well as the characterization of the unsteady boundary layer developed on an ascillating airfoil. However, the acquisition of the surface pressure distribution usually requires the necessity of fabrication of a large number of pressure orifices, and the installation of the associated miniature transducers on the airfoil model. Furthermore, the surface pressure distribution method could suffer from somewhat limited spatial resolution and transducer response. More convenient and practical means capable of determining the detailed unsteady boundary-layer events on the entire unsteady aerodynamic objects both nonintrusively and simultaneously would be advantageous.

The objectives of this study were to examine nonintrusively the unsteady boundary layer developed on the upper surface of a NACA 0012 airfoil model oscillated sinusoidally within and beyond the static-stall angle using closely-spaced, multiple hot-film sensor (MHFS) arrays. Special emphases were placed on the measurements of the unsteady effects on the spatial-temporal movements of the leading-edge stagnation point, flow separation and reattachment points, the boundary-layer transition and relaminarization, and flow reversal. Hot-wire anemometry and smoke-tunnel flow visualization were also made to supplement the MHFS measurements. These measurements were also used to postulate the mechanisms responsible for the behavior of these boundary-layer events, and to add knowledge for understanding the unsteady separated flows developed on aerodynamic objects related to helicopter rotors, propellers, and fixed wings.

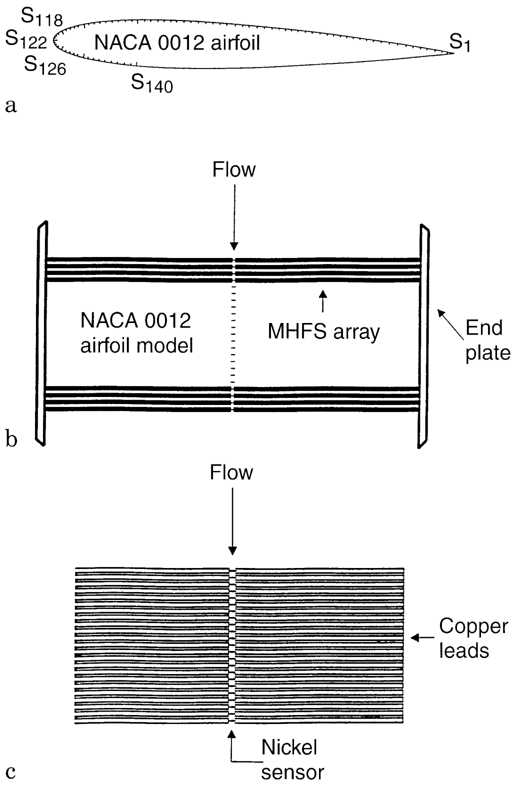

Fig. 1. Schematics of **a** NACA 0012 airfoil model, and **b**–**c** MHFS pattern and the layout of the copper leads

2
Experimental Methods and Apparatus

2.1
Flow facility and airfoil model

The experiments were performed in the 17 in × 30 in × 6 ft low-speed, suction type wind tunnel in the Aerodynamics Laboratory in the Department of Mechanical Engineering of McGill University. The free-stream turbulence intensity was 0.25% at $U_0 = 17.3$ m/s, and the flow nonuniformity was less than 1%. A NACA 0012 airfoil, fabricated from solid aluminum, with a chord length (C) of 15 cm and a span of 37.5 cm was used in the investigation (Fig. 1a). The airfoil was mounted horizontally on a steel shaft and connected to the stepper motor through a cam-arm system. The airfoil was driven in a sinusoidal motion ($\alpha(t) = \alpha_0 + \Delta\alpha \sin 2\pi f_0 t$, where α_0 is the mean angle of attack, $\Delta\alpha$ and f_0 are the oscillation amplitude and frequency, respectively) by a programmable control system. The computer control algorithm generated independent, preprogrammed pulse trains that determined the driving stepper motor shaft displacement and rate histories. The airfoil pitch axis was located at $\frac{1}{4}$-chord throughout the experiment. The phase reference signal, (φ) and $\alpha(t)$ of the airfoil were monitored through a potentiometer (TRW type DP 801) with an accuracy of $\pm 0.1°$. Figure 2 shows the typical time histories for a measured sinusoidal oscillation. In the present experiment, the free-stream velocity was held constant at $U_0 = 17.3$ m/s which renders a chord Reynolds number (Re) of 169,000. The airfoil model was oscillated within ($\alpha = 0 + 7.5° \sin \omega t$) and beyond ($\alpha = 7.5° + 7° \sin \omega t$) the static-stall angle (α_{SS}), respectively, with $f_0 = 2$ and 4 Hz or a reduced frequency, κ ($= \pi f_0 C / U_0$), of 0.053 and 0.109. The oscillation frequency was measured to an accuracy of ± 0.02 Hz. Also, in the following discussion, the suffix u is used to indicate pitchup when α is increasing and d is used to indicate pitchdown when α is decreasing.

The wake of the airfoil model was examined by using a hot-wire probe (DISA P11) with a Dantec 56C17 constant-temperature anemometer (CTA). The overheat ratio was set at 1.8. The hot-wire probe was mounted on a sting extended from a computer-controlled 2-D traversing mechanism. The probe was moved with accuracy in the x and y directions with 20 and 25 μm, respectively. All hot-wire calibrations, mean-flow measurements, free-stream turbulence levels, rms-disturbances measurements, and subsequent processing were performed on a 486 PC with a 12 bit A/D converter board

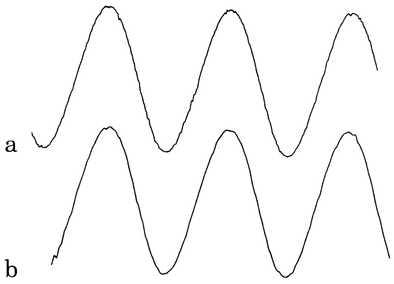

Fig. 2a, b. Typical sinusoidal oscillation waveforms. Upper trace: airfoil angular position from the output of a potentiometer. Lower trace: reference signal from a function generator

(Computer Boards model Das16/330), using the Streamer data acquisition software. The hot-wire signals were sampled at 2 kHz and fed simultaneously to a FFT analyzer to extract the frequency of the vortex shedding directly.

The flow structures above the NACA 0012 airfoil with $C = 12.5$ cm were visualized by using a smoke tunnel. A similar oscillation mechanism was also built so as to reproduce the oscillatory motion imposed on the NACA 0012 airfoil in the smoke tunnel. The visualized wake structures at different angles of attack were recorded with a 60 Hz video camera together with a 35 mm still camera using Kodak ASA 3200 color film and a shutter speed of 1/1000 s. The oscillation frequency was fixed at 1 Hz which corresponded to a κ of 0.0655.

2.2
Multiple hot-film sensor (MHFS) arrays

The MHFS array used in this study consists of a number of thin nickel films (0.2 μm), which are electron-beam evaporated onto a thin polyimide substrate (50 μm) in a straight-line array. Each sensor consists of a nickel film 2.5 mm long and 0.1 mm wide with 10-μm copper-coated nickel leads routed to provide wire attachment away from the measurement location. The nominal resistance of the sensor is 18 Ω. The entire sensor array consists of 140 sensors spaced at $S = 1.30$ mm apart with sensor S_{122} located at the leading-edge stagnation point (LESP) of the airfoil. Sensors S_1 and S_{121} were on the entire upper surface and sensors S_{123}–S_{140} were on the lower surface of the airfoil. The sensor number indicates the location of the hot-film sensors along the surface of the airfoil, and is proportional to the distance covered along the lower and upper surface of the airfoil from the leading edge. The sensor array was bonded onto the entire airfoil contour using double-sided mylar adhesive tape, which prevented the sensor array from introducing surface irregularities to the model surface. Figs. 1b and c show the sensor pattern and the layout of the copper leads.

Groups of 14 of the 140 sensors were systematically connected to 14 CTAs (AA Lab model AN-1003) to obtain the time history of the heat transfer output at each sensor position. The sensors were connected to the CTAs using magnet wire and BNC coaxial cable combination to minimize the disturbance to the flow in the tunnel test section. The overheat ratio was set at 1.09 which ensures that only a small amount of heat was introduced, and that the heated thin films caused little disturbance to the shear layer or to each other. This was checked by heating the films individually and in groups while monitoring the effects on other films. CTA output signals were low-pass filtered and amplified by a gain between 10 and 50. The sensors were uncalibrated. The overheat ratio, DC offset, and the amplifier gain for each sensor were carefully adjusted such that each sensor was at nearly the same operating conditions. For each set of data, 14 CTA channels from the MHFS and one CTA channel from the hot-wire probe were simultaneously sampled and digitized at 2 kHz per channel by the data acquisition system described in Sect. 2.1. The output signals from the potentiometer were also sampled and serve as reference signals between each set of CTA output signals. The amplified signals were also connected to a four-channel oscilloscope (LeCroy model 9304) to provide on-line time history traces of the operating group of sensors.

No calibration of the MHFS was performed as the objective of this experiment was to document the qualitative behavior of the boundary layer shear stress characteristics. Therefore, the heat transfer or the voltage output level of the heated hot-film sensor gives a direct recognition of the state of the boundary layer over it. The laminar and transitional flows are indicated by a low heat transfer and a rapid rise in heat transfer, respectively. Separation is indicated by a low level of average heat transfer. It is worth noting that the qualitative extraction of the state of the boundary layer also relieves the great difficulty encountered in the calibrating of multiple surface-mounted hot-film sensors (Lorber and Carta 1992). These difficulties are attributed to the need to either (i) calibrate all probes in a reference unsteady flow before installation, (ii) provide a reference flow at each sensor, or (iii) calibrate the sensors by composition to a traceable and portable reference probe. The other constraint in the use of surface-mounted hot-film sensors, i.e., the influence of non-negligible heat transfer through polyimide substrate to the model and the fluid, which has been found to be significant in quantitative measurements in air flow (e.g., Alfredsson et al. 1988; Diller and Telionis 1989; Cook 1991), was not believed to be a problem in the present method.

3
Results and discussion

3.1
Stationary airfoil

To facilitate the characterization of the unsteady effects on the development of the boundary layer on an oscillating NACA 0012 airfoil model, the laminar separation and transition points and the onset of flow reversal were measured first using MHFS together with the smoke-tunnel flow visualizations with the airfoil held at various angles of attack with $Re = 169000$ (Fig. 3). Figure 3 summarizes the MHFS determination of the locations of the laminar separation points at different angles of attack (open triangles), which indicates that the laminar separation bubbles moves rapidly toward the leading edge with increasing α. The identification of the laminar separation point was based on the 180° phase shift phenomenon (PSP), due to the presence of flow bifurcation observed by Stack et al. (1987), across the simultaneously recorded MHFS outputs (see Fig. 4).

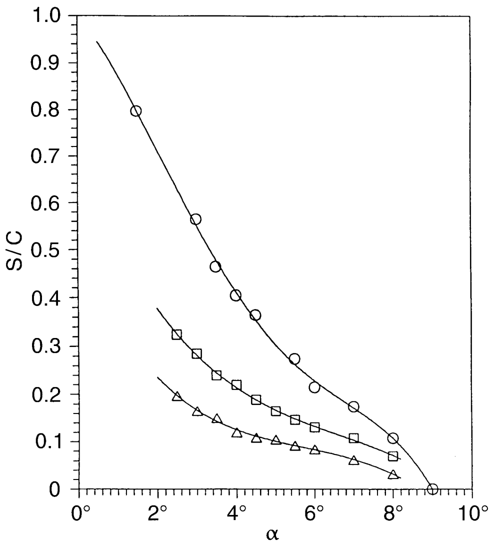

Fig. 3. Locations of laminar separation and transition points, and the onset of flow reversal on a stationary NACA 0012 airfoil at different angles of attack. △, laminar separation point; □, peak transition point; and ○, onset of flow reversal

Figure 4 shows the selected time histories of S_{110}–S_{106} outputs for $\alpha = 4.5°$. It reveals that, even in a visual comparison, there is a PSP across S_{107} and S_{108}, which allows the detection of the laminar separation bubble around S_{108} (at $S/C = 0.121$). The existence of the PSP can also be confirmed from the coherence obtained by cross-correlating the simultaneously recorded MHFS outputs across the points of interest. The PSP also allows the detection of the stagnation and reattachment points. However, due to the large spanwise movement of the turbulence, the determination of turbulent reattachment of laminar separation bubble and the onset of turbulent flow reversal on a stationary airfoil was not satisfactory. MHFS array with improved spatial resolution is needed to measure successfully the turbulent separation and reattachment points. However, it is worth noting that interpretation of hot film signals is more straightforward for periodic unsteady flows because the changes from one flow state to another can be more readily identified (as shown in Figs. 6 and 11 below) than the characteristics of a steady-state flow.

Figure 3 also shows the MHFS measurements of locations of laminar-to-turbulence transition on a stationary NACA 0012 airfoil model with α (open squares). The transition point moved forward with increasing α which implies that the separation bubble became narrower and moved closer to the leading edge with increasing α. The transition points shown in this figure corresponded to the sensor location at which the sensor output presented a peak transition. The MHFS determination of the onset and end of transition, generally covering about 2–4% chord region, is shown in Fig. 5.

Figure 5 shows the selected normalized sensor outputs representing a typical sequence of boundary-layer transition for $\alpha = 4.5°$. The low normalized sensor outputs (S_{114} and S_{110}) indicate that the boundary layer was laminar (Figs. 5a and b). As the boundary layer became unstable, periodic turbulent bursts began to appear with associated increase in the outputs of sensors S_{104} and S_{103} (Figs. 5c and d). The sensor output level (S_{100} or $S/C = 0.19$) reached a maximum at peak transition (Fig. 5e). It followed by a slight decrease, as a consequence of the thickening of the boundary layer, in the output level at S_{88} in the turbulent region (Fig. 5f). The demarcation of the laminar, transitional, and turbulent regions can also obtained from the one or more of the following criteria: the variations of rms of the sensor output, intermittency factor, and the frequency contents of the MHFS outputs. The transition point can also be determined from the ensemble-averaged “quasi-steady” voltage levels from each sensor over many subintervals. Each subinterval corresponded to one static angle of attack (Lorber et al. 1992; Schreck et al. 1994).

Figure 3 also shows the flow visualization results of the location of the onset of flow reversal or the point of trailing-edge separation with α (open circles). This figure shows that the onset of flow reversal progressed smoothly toward the leading edge with increasing α, which indicates that the static still occurred by the mechanism of the smooth upstream movement of trailing-edge separation. The α_{SS} was found to be around 9°.

3.2
Oscillating airfoil

Figures 6 and 11 show the composite plots of time traces of MHFS measurements (S_{136}–S_1) of the unsteady boundary layers developed on the upper surface of a NACA 0012 airfoil oscillated within and beyond α_{SS}, respectively, with $\kappa = 0.109$ and $Re = 169\,000$. The numbers shown on the right side ordinate axes in these figures correspond to sensor numbers on the airfoil model. The lowermost curve represents the variation in the potentiometer voltage which indicated the location of

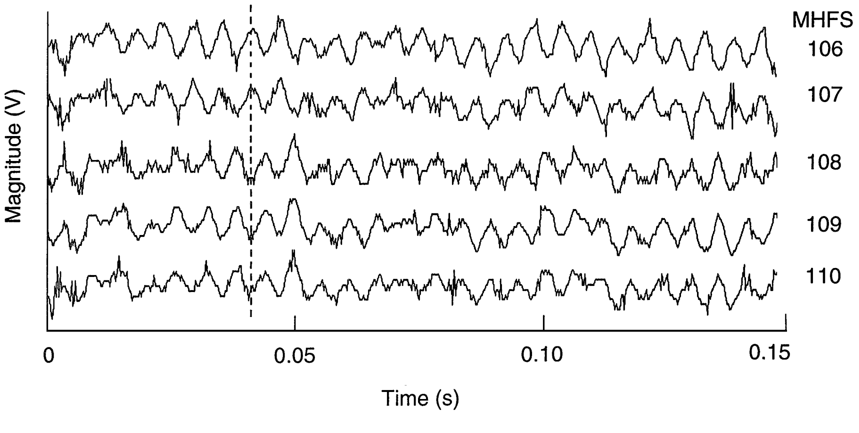

Fig. 4. Typical MHFS outputs for a airfoil positioned at $\alpha = 4.5°$ with $Re = 169000$. Note the presence of 180° phase difference between S_{107} and S_{108} which allows the identification of laminar flow separation point at around S_{108}

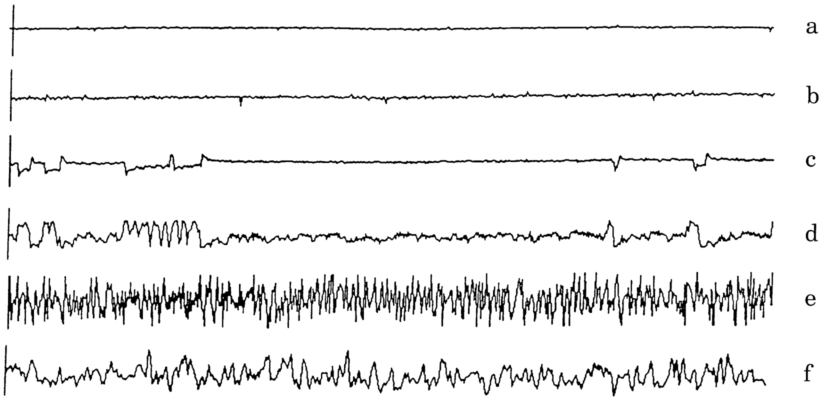

Fig. 5a–f. Selected normalized MHFS outputs showing the onset and end of laminar-to-turbulence transition for $\alpha = 4.5^\circ$ and $Re = 169000$. **a** and **b** indicate laminar boundary layer at S_{114} and S_{110}; **c**–**d** indicate laminar with turbulent bursts at S_{104} and S_{103}; **e** indicate peak transition at S_{100}; and **f** indicates turbulent boundary layer at S_{88}

a reference sensor on the model at a given instant. The y-axis represent the voltage output level of each sensor. The outputs were self-scaled to a peak-to-peak value of one which allows the regions of change to be easily identified and provides a clear qualitative picture. The repeatability from cycle to cycle was found extremely good, and for clarity only one cycle needed to be shown.

3.2.1
Airfoil oscillated within α_{SS} ($\alpha = 0^\circ + 7.5^\circ \sin \omega t$)

Figure 6a shows the time histories of S_{112}–S_{126} outputs in the leading-edge region of a NACA 0012 airfoil oscillated within α_{SS} with $\alpha_0 = 0^\circ$, $\Delta\alpha = 7.5^\circ$, and $\kappa = 0.109$. The movement of the LESP with $\tau(=\omega t)$ or α (indicated by the locus of LESP) is clearly indicated by the travel of the minimum voltages from outputs of S_{118}–S_{126} during one cycle of oscillation. Sensor S_{118} at time instant T_1 traverses the instantaneous LESP first followed by sensors S_{119}–S_{126} (at T_2–T_9) during pitchup, and then followed by sensors S_{126}–S_{118} (at T_9–T_{17}) during pitchdown. The spatial-temporal progression of LESP with α was summarized in Fig. 7 (solid circles). The identification of the stagnation point using MHFS can be used to determine the wing angle of attack and provide wing stall warning. Furthermore, it is worth noting that the identification of the instantaneous location of the stagnation point can also be obtained directly based on the presence of PSP across the time instants shown in Fig. 6a. The PSP determination of the stagnation point provides an alternative method in addition to the direct recognition (based on the sensor output levels as described in Fig. 6a), which requires the somewhat time-consuming adjustment of a bank of CTAs so as to ensure that each sensor is operated at the same operating conditions.

Also, it is interesting to note that the model motion (or the maneuver frequency) of the airfoil can also be picked up from the MHFS outputs in the leading-edge region of the oscillating airfoil model. Figure 8 shows that by low-pass filtering the outputs of S_{118} and S_{126}, the flow unsteadiness caused by boundary (body) oscillation (indicated by the mean voltage signals) and by the flow disturbances (indicated by the fluctuating voltage signals) can be captured simultaneously. The MHFS acquisition of the spatial-temporal variations of flow unsteadiness and flow instability simultaneously is especially useful in the study of an aeroelastic system, such as a wing or helicopter rotor blade with torsional instability (Lorber et al. 1992, 1994).

The effects of the small-amplitude oscillation on the unsteady boundary-layer events occurred on the upper surface of the NACA 0012 airfoil are illustrated in Fig. 6b. Fig. 6b shows that the spatial-temporal movement of the laminar separation point (indicated by the line of laminar separation) during pitchup, and reattachment point (indicated by the line of reattachment) during pitchdown were identified directly based on the local minimum in the outputs of S_{114}–S_{110}. The unsteady effects on the onset of the laminar separation and reattachment points were summarized in Fig. 9 (circular symbols). Figure 9 reveals that the onset of the laminar separation point was delayed to higher angles of attack compared to the static results. The laminar separation point moved forward rapidly when the airfoil is near the apex of its motion, and the reattachment point moves rearward at $\alpha(t)$ is decreasing. The laminar bubble first occurs at $\alpha_u = 6.1^\circ$ (S_{114}), and reattaches at $\alpha_d = 5.3^\circ$ during one cycle of oscillation. This compares with the predicted static value of 7° at same $S/C = 0.07$ which indicates the delay of the laminar separation (due to the unsteady moving-wall and accelerated flow effects). Figure 6b also indicates that the asymmetry is always present for separation and reattachment during pitchup and pitchdown motion of the airfoil.

Figure 6b also shows that the spatial-temporal progression of the onset of unsteady boundary-layer transition (indicated by a sharp increase in the heat transfer) during pitchup, and relaminarization (indicated by a decrease in the heat transfer) during pitchdown can be recognized clearly from the MHFS (S_{109}–S_1) data. Transition was initially observed at the sensor farthest aft (S_1) and progresses forward with increasing α. The onset of transition (relaminarization) was delayed (promoted) which caused a shorter (longer) attached turbulent flow on the pitchup (pitchdown) NACA 0012 airfoil model oscillated within α_{SS}. The turbulent flow remained fully attached to the airfoil (at least up to S_3) which clearly illustrates the favorable effects of oscillatory forcing in keeping the boundary layer attached to the airfoil to much higher angles of attack than could be attained under static conditions. The drop in the outputs of sensors (S_3–S_1 or $S/C = 1.03$–1.05) near the trailing edge (at $\alpha_d \approx 7^\circ$ and designated by points 1, 2, and 3) may imply the onset of the trailing-edge separations, which were

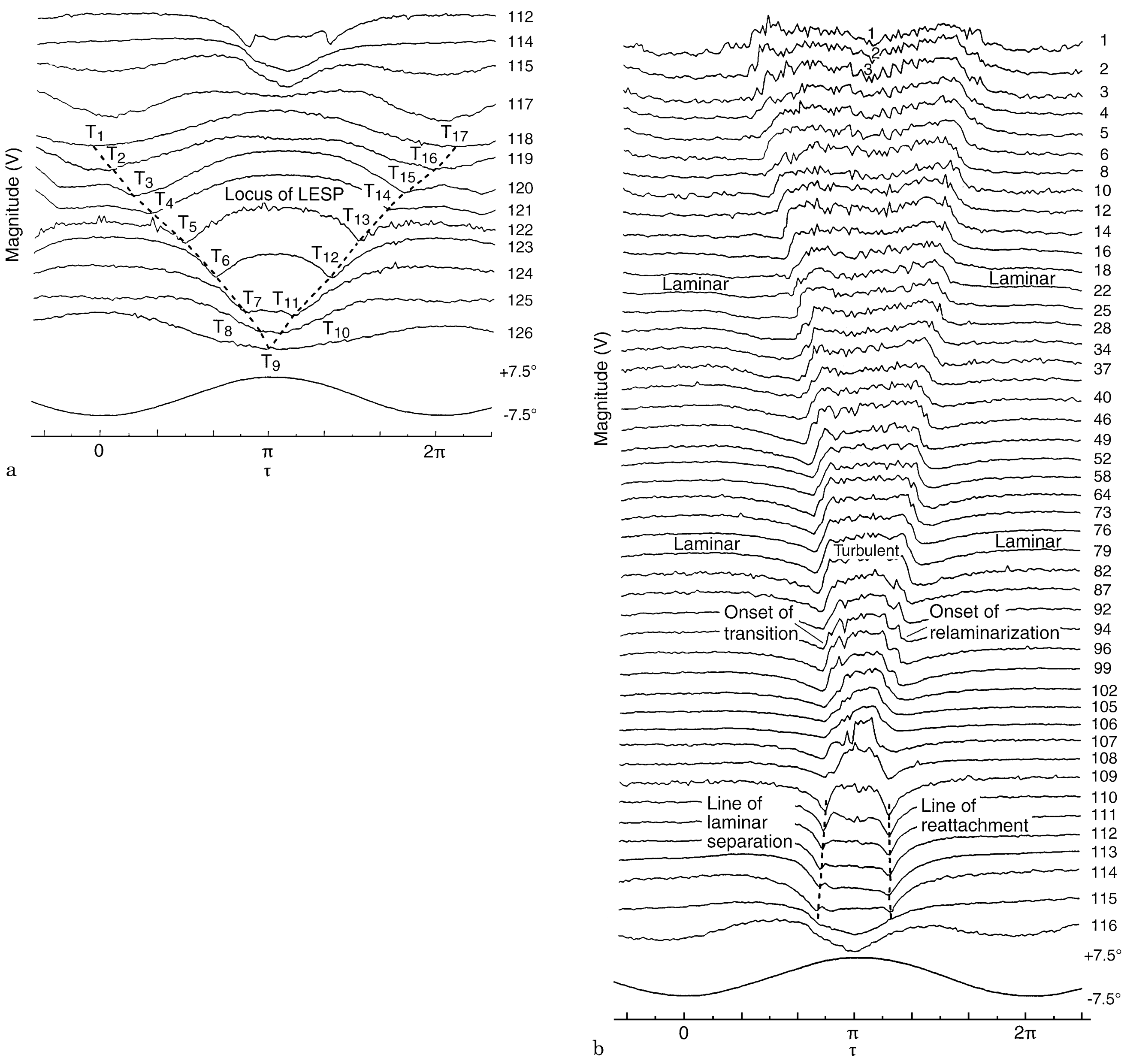

Fig. 6a,b. Composite plots of selected simultaneously acquired MHFS signals on an oscillating NACA 0012 airfoil with $\alpha_0 = 0^\circ$, $\Delta\alpha = 7.5^\circ$, $\kappa = 0.109$, and $Re = 169\,000$. **a** S_{126}–S_{112}, **b** S_{116}–S_1

significantly delayed due to the unsteady effects. The effects of unsteady motion on the onset of boundary-layer transition and relaminarization with α at different κ were summarized in Fig. 10.

Figure 10 shows that the onset of the unsteady boundary-layer transition was delayed relative to the static case (open squares in Fig. 3); i.e., they occur farther from the leading edge for a given value of α, or larger incidence for a given *S*/*C*. The unsteady transition delay could be attributed to the convective time lag and the boundary-layer improvement in unsteady motions as suggested by Ericsson and Redding (1988), and Ericsson (1993). The transition point moved toward the leading edge with increasing α_u, and at a given chordwise position relaminarization generally occurred at a lower α than transition. Figure 10 also shows that the primary effect of increasing the oscillating frequency is to delay the forward motion of the transition point. The delay of the transition was reduced with decreasing κ. Figure 10 also reveals that there is a hysteresis (asymmetry) in the transition-relaminarization cycle which decreased with decreasing κ. The hysteresis decreases at higher α, as the transition point approaches the leading edge.

3.2.2
Airfoil oscillated beyond α_{ss} ($\alpha = 7.5^\circ + 7^\circ \sin \omega t$)

Figures 11a, b and c show the MHFS (S_{136}–S_1) outputs illustrating the effects of large amplitude oscillation on the behavior of the unsteady boundary layer developed on the

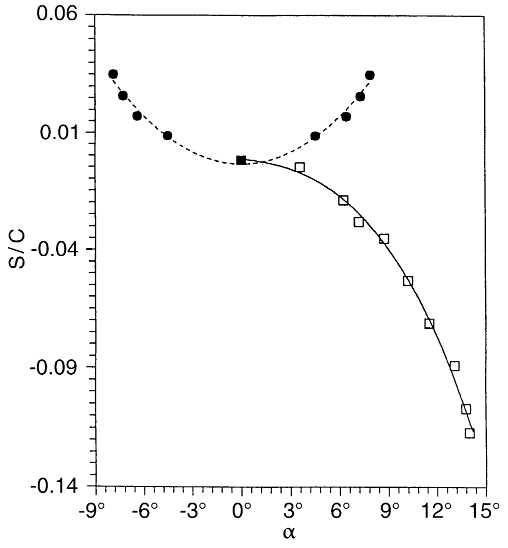

Fig. 7. Variation of LESP with α for $\kappa=0.109$. ●, $\alpha(t)=0°+7.5° \sin \omega t$; □, $\alpha(t)=7°+7° \sin \omega t$

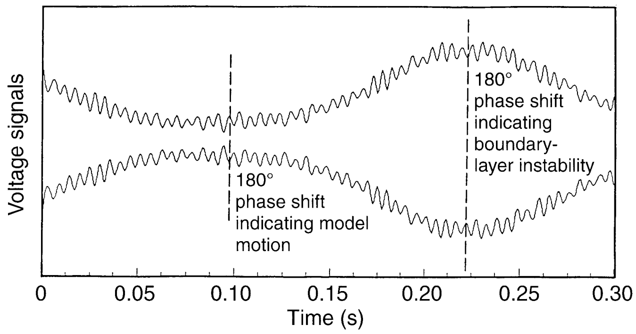

Fig. 8. Low-pass filtered signals of sensors S_{118} (top voltage–time trace) and S_{126} (bottom voltage–time trace). Note the phase difference of 180° between the mean and fluctuating voltage outputs of these two sensors

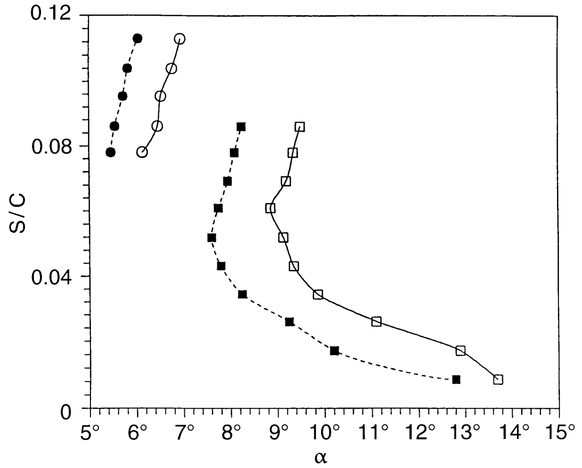

Fig. 9. Variations of laminar separation and reattachment points with α for $\kappa=0.109$. $\alpha(t)=0°+7.5° \sin \omega t$; ○, laminar separation; ●, reattachment. $\alpha(t)=7.5°+7.5° \sin \omega t$: □, laminar separation: ■, reattachment

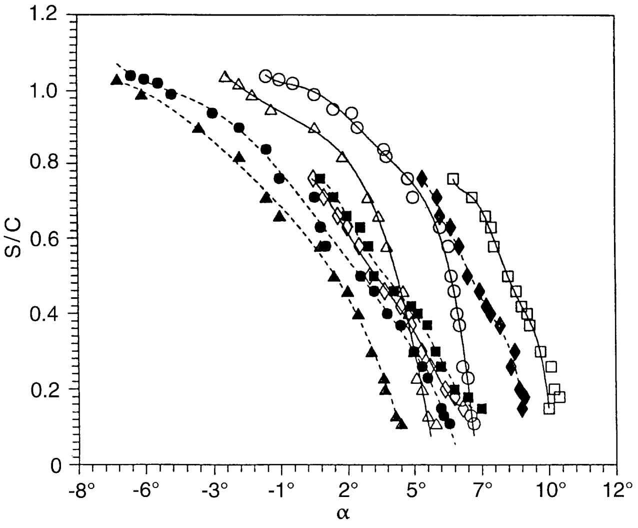

Fig. 10. Variations of the onset of boundary-layer transition and relaminarization with α and κ. Transition: ($\alpha(t)=0°+7.5° \sin \omega t$) ●, $\kappa=0.0535$; ○, $\kappa=0.109$ and ($\alpha(t)=7.5°+7° \sin \omega t$) ■, $\kappa=0.0535$; □, $\kappa=0.109$. Relaminarization: ($\alpha(t)=0°+7.5° \sin \omega t$) ▲, $\kappa=0.053$; △, $\kappa=0.109$ and ($\alpha(t)=7.5°+7° \sin \omega t$) ◇, $\kappa=0.053$; ◆, $\kappa=0.109$

upper surface of the NACA 0012 airfoil model oscillated with $\alpha_0=7.5°$, $\Delta\alpha=7°$, and $\kappa=0.109$. The movement of the stagnation point (indicated by the locus of LESP) was again determined based on the local minimum in the sensor outputs (S_{122}–S_{136}) shown in Fig. 11a and summarized in Fig. 7 (open squares). Figure 11b also shows that the movements of the laminar separation and reattachment points (between S_{121} and S_{112}), and the rear-to-front progression of the unsteady boundary-layer transition and relaminarization (between S_{111} and S_{28}) with α are qualitatively quite similar to the results shown in Fig. 6b. That is, the laminar separation and transition were delayed with increasing α, and the reattachment and relaminarization were promoted with decreasing α. Also, similar to the case of small-amplitude oscillation, the onset of the unsteady boundary-layer transition and relaminarization were delayed to higher angles of attack as κ increases (Fig. 10). However, it was found that, compared with the results for low amplitude oscillation, the onset of the laminar separation bubble was sustained to higher angles of attack with longer bubble. Also, the hysteresis developed between the values of α for transition and relaminarization (up to 1.85°) is smaller compared with those observed for low amplitude oscillation (up to 0.8°). The hysteresis is much stronger near the trailing edge (which could be attributed to the flow separation) than it is closer to the leading edge.

Figures 11b and c show that the turbulent flows, especially near the trailing edge (S_{25}–S_1), have an increased turbulence fluctuations, and that they are largely separated. The various stall events, e.g., unsteady boundary-layer separation (leads up to the dynamic stall), and reattachment (due to the passage of the vortex disturbance during stall) are indicated in Fig. 11b. The primary differences (compared to oscillation within α_{SS}) are starting at S_{111} ($S/C=0.095$), at which a sudden change in the output (at point 5) indicates a group change in the flow structure over the airfoil. For clarity, the surface-flow measurements at S_{106} were selected to illustrate the various stall events.

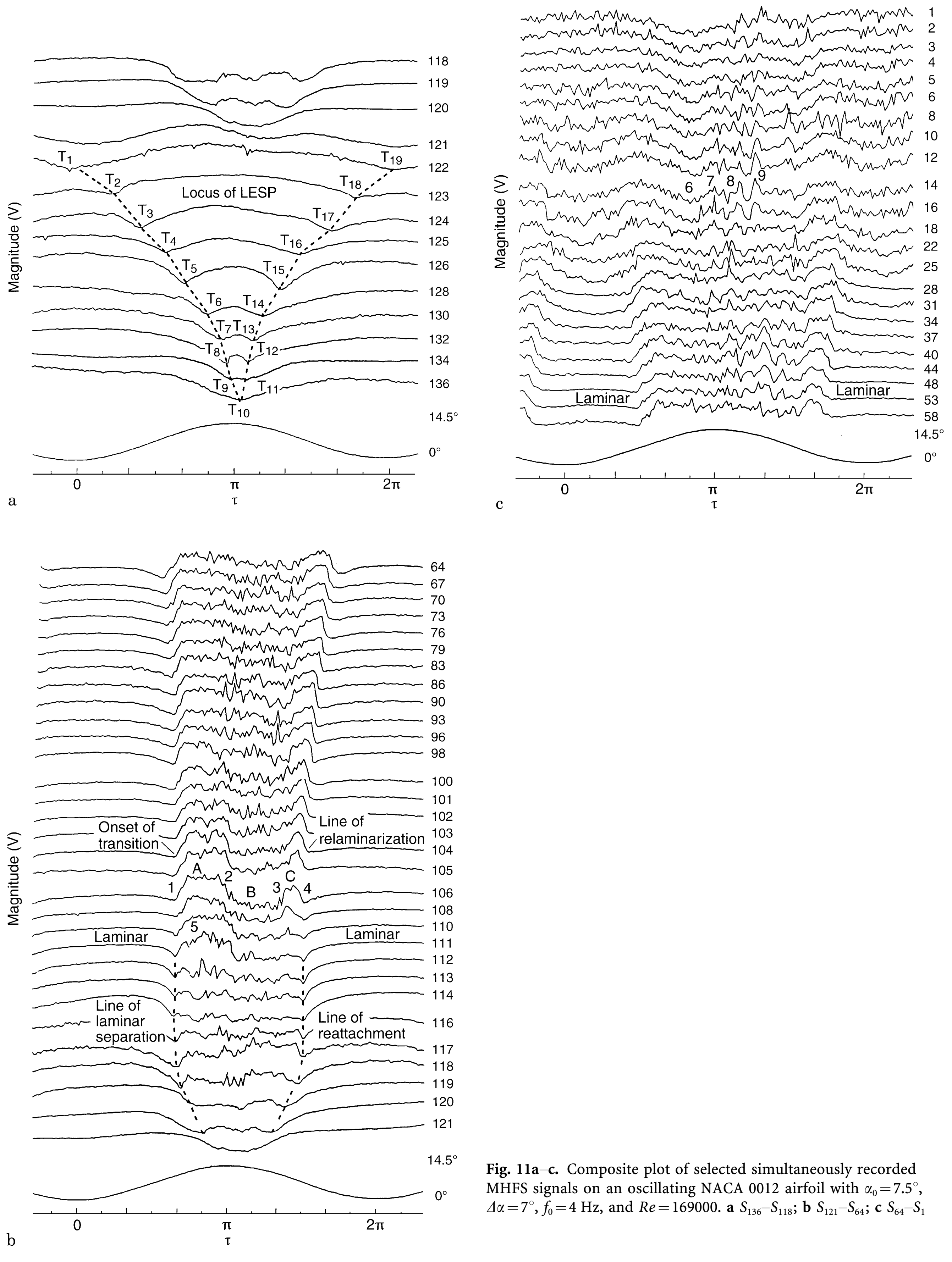

Fig. 11a–c. Composite plot of selected simultaneously recorded MHFS signals on an oscillating NACA 0012 airfoil with $\alpha_0=7.5°$, $\Delta\alpha=7°$, $f_0=4$ Hz, and $Re=169000$. **a** S_{136}–S_{118}; **b** S_{121}–S_{64}; **c** S_{64}–S_1

At S_{106} ($S/C = 0.139$), the unsteady boundary layer remained laminar between $\alpha_u = 0°$ to $10.6°$ and became turbulent starting at $\alpha_u = 11.7°$ (point 1). The turbulent boundary layer ($\alpha_u = 11.7°$ to $\approx 13.5°$ designated by region A) then broke down abruptly (indicated by a drop in the sensor outputs) at $\alpha_u \approx 13.5°$ (point 2). The separated boundary layer ($\alpha_d \approx 14°$ to $\alpha_d \approx 10.6°$, region B) then reattached to the airfoil surface (indicated by an increase in heat transfer) at $\alpha_d \approx 9.5°$ (point 3). The high level in sensor outputs indicates that the flow reattached as a turbulent boundary layer ($\alpha_d \approx 9.5°$–$7.6°$, region C). The subsequent drop in heat transfer corresponds to a relaminarization of the boundary layer at $\alpha_d \approx 6.9°$ (point 4). Region B suggests the formation and shedding of a vortex-like disturbance (from the leading edge region of the airfoil) at S_{106} and began to move rearward. The stall process in the leading-edge region is characterized with a forward of the turbulent separation as the maximum incidence ($\alpha = 14.2°$) was approached, complete stall for a brief period, and reattachment of the boundary-layer flow progressed rearward from the leading-edge during the pitchdown.

Figure 11c also indicates that all the other sensors downstream of around S_{25} ($S/C = 0.841$) showed a less abrupt change in output either slightly before or after the turbulent breakdown at S_{109} (at $\alpha_u \approx 14.2°$ or $\tau \approx \pi$; designated by point 5). For clarity, referring to S_{14}, it can be seen that a minimum in the sensor output was obtained ($\alpha_u \approx 12.8°$ at point 6), which could imply a change in the flow direction, or that flow reversals may be taking place within the boundary layer in the absence of any significant flow separation. It is significant that these flow reversals occurred before the onset of leading edge separation ($\alpha_u \approx 14.2°$ at point 5). Point 6 was then followed by an increase in the output (point 7 at $\alpha_d \approx 14.1°$) which suggests the passage of the vortex across the chord during the dynamic stall. After the passage of the primary vortex, the peaks in the output (points 8 and 9 at $\alpha_d \approx 12.4°$ and $11.2°$, respectively) indicate the passage of a weaker secondary vortex. Figures 11b and c suggest that the dynamic stall process was initiated by the turbulent flow separation, indicated either by an abrupt breakdown of the turbulent flow (point 5) or by a less abrupt drop in output level to a distinct minimum value as the flow reverses (point 6). A dynamic stall angle of about $14.2°$ was observed compared to $\alpha_{SS} = 9°$. Figure 11b also reveals that the dynamic stall significantly changes transition location on a pitching airfoil, i.e., the transition has moved very close to the leading edge by $\alpha = 9.8°$, well before the onset of turbulent separation at $\alpha_u \approx 14.2°$. The onsets of the leading-edge turbulent breakdown and the trailing-edge flow reversal with α and κ are summarized qualitatively in Fig. 12 (rhombus symbols). Note that only the identifiable flow separation points were plotted.

Figure 12 shows that (i) as α increased, the flow separation moved very quickly to the leading-edge, (ii) increasing κ delayed the turbulent breakdown and the onset of flow reversal to higher angles of attack, and (iii) the vortex remains on the upper surface (S_{111}–S_{25}) until reaching higher angles of attack which are considerably higher than the static stall angles (open triangles). That is, for an airfoil oscillated beyond α_{SS}, the flow remained attached to the airfoil surface to angles of attack much higher than could be attained statically. Figure 12, together with Fig. 10, indicates that the unsteady boundary layer transition consistently precedes both unsteady turbulent boundary layer reversal and leading edge vortex initiation. Figure 12, together with Fig. 9, suggests that a short laminar separation bubble was observed to precede stall, which implies that the dynamic stall process might not originate with the bursting of a laminar separation bubble, but with a breakdown of the turbulent boundary layer (McCroskey et al. 1976).

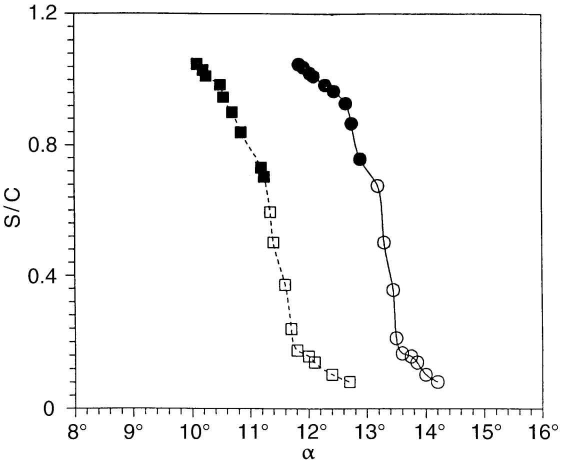

Fig. 12. Variations of the onset of flow reversal and turbulent reattachment with α and κ for $\alpha(t) = 7.5° + 7° \sin \omega t$. Turbulent breakdown: □, $\kappa = 0.053$; ○, $\kappa = 0.109$. Flow reversal: ■, $\kappa = 0.053$; ●, $\kappa = 0.109$

4
Conclusions

The spatial-temporal progressions of the stagnation, separation, and reattachment points, and the state of the unsteady boundary layer developed on the upper surface of a NACA 0012 airfoil oscillated sinusoidally within and beyond the static stall angle of attack were measured nonintrusively using closely-spaced, multiple, hot-film sensor (MHFS) arrays. The MHFS measurements also indicate that (i) the separation and transition were delayed with increasing α and the relaminarization and reattachment of the unsteady boundary layer were promoted with decreasing α, relative to the static case, due to the unsteady motion, (ii) the pitchup motion helps to keep the boundary layer attached to higher angles of attack over that could be obtained statically, (iii) the dynamic stall process was initiated by the turbulent flow separation in the leading-edge region as well as by the onset of flow reversal in the trailing-edge region, (iv) the unsteady boundary layer transition consistently precedes both unsteady boundary layer reversal and leading edge vortex initiation, and (v) the dynamic stall process was found not to originate with the bursting of a laminar separation bubble, but with a breakdown of the turbulent boundary layer. The MHFS results also show that both the flow unsteadiness caused by model motion and by flow disturbances can be detected simultaneously. Further measurements, especially the effects of oscillation frequency and amplitude, are needed to better characterize the unsteady separated flows and the details of the mechanism lead to dynamic stall by the use of MHFS arrays.

References

Acharya M; Metwally MH (1992) Unsteady pressure field and vorticity production over a pitching airfoil. AIAA J 30(2): 403–411

Alfredson PH; Johansson AV; Haritonidis JH; Eckelmann H (1988) The fluctuating wall-shear stress and the velocity filed in the viscous sublayer. Phys Fluids 31(5): 1026–1033

Bellhouse BJ; Schultz DL (1966) Determination of mean and dynamic skin friction, separation and transition in low-speed flow with a thin-film heated element. J Fluid Mech 24: 379–400

Carr LW (1987) Progress in analysis and prediction of dynamic stall. J Aircraft 25(1): 6–17

Carta FO; Lorber PF (1987) Experimental study of the aerodynamics of incipient torsional stall flutter. J Propulsion and Power 3(2): 164–170

Chandrasekhara MS; Ahmed S (1991) Laser velocimetry measurements of oscillating airfoil dynamic stall flow field. AIAA Paper 91-1799

Cook W (1991) Response of hot element wall shear stress gages in unsteady turbulent flows. AIAA Paper 91-0167

Daley DC; Jumper EJ (1984) Experimental investigation of dynamic stall for a pitching airfoil. J Aircraft 21: 831–832

Diller TE; Telionis DP (1989) Time-resolved heat transfer and skin friction measurements in unsteady flow. In: Advances in Fluid Mechanics Measurement, ed. M. Gad-el-Hak, 321–355

Ericsson LE; Reding JP (1988) Fluid mechanics of dynamic stall. Part I. Unsteady flow concept. J Fluids Struc 2: 1–33

Ericsson LE (1993) The moving wall effect vis-à-vis other dynamic stall flow mechanisms. AIAA Paper 93-3424-CP

Favier D; Agnes A; Barbi C; Maresca C (1988) Combined translational/pitch motion: a new airfoil dynamic stall simulation. J Aircraft 25: 805–814

Koochesfahani MM (1989) Vortical patterns in the wake of an oscillating airfoil. AIAA J 27: 1200–1204

Lorber PF; Carta FO; Covino AF (1988) Airfoil dynamic stall at constant pitch rate and high Reynolds number. J Aircraft 25: 548–556

Lorber PF; Carta FO; Covino AF (1992) An oscillating three-dimensional wing experiment: compressibility, sweep, rate, and geometry effects on unsteady separation and dynamic stall. United Technologies Research Center Rept. R92-958325-6, East Hartford, Connecticut, USA

Lorber PF; Carta FO (1994) Incipient torsional stall flutter aerodynamic experiments on three-dimensional wings. J Propulsion and Power 10: 217–224

McAlister KW; Carr LW (1979) Water tunnel visualizations of dynamic stall. J Fluids Eng 101: 376–380

McCroskey WJ; Carr LW; McAlister KW (1976) Dynamic stall experiments on oscillating airfoils. AIAA J 14: 57–63

McCroskey WJ (1977) Some current research in unsteady fluid dynamics. J Fluids Eng 99: 8–38

McCroskey WJ; McAlister KW; Carr KW; Pucci SL; Lamber SL; Indergrand RF (1981) Dynamic stall on advanced airfoil sections. J AM Helicopter Soc 26: 40–50

McCroskey WJ (1982) Unsteady airfoils. Ann Rev Fluid Mech 14: 285–311

Ohmi K; Coutaneau M; Daube O; Loc TP (1991) Further experiments on vortex formation around an oscillating and translating airfoil at large incidences. J Fluid Mech 225: 607–630

Owen FK; Bellhouse BJ (1970) Skin friction measurements at supersonic speeds. AIAA J 8: 518–532

Schreck S; Faller W; Helin H (1994) Pitch rate and Reynolds number effect on unsteady boundary layer transition and separation. AIAA Paper 94-2256

Stack JP; Mangalam SM; Berry SA (1987) A unique measurement technique to study laminar-separation bubble characteristics on an airfoil. AIAA Paper 87-1271